ACS NANO

www.acsnano.org

ARTICLE

Directional Coupling to a λ/5000 Nanowaveguide

Alessandro Tuniz,* Sabrina Garattoni, Han-Hao Cheng, and Giuseppe Della Valle

Cite This: *ACS Nano* 2024, 18, 30626–30637

Read Online

ACCESS | Metrics & More | Article Recommendations | Supporting Information

ABSTRACT: **Silicon-based microdevices are considered promising candidates for consolidating several terahertz technologies into a common and practical platform. The practicality stems from the relatively low loss, device compactness, ease of fabrication, and wide range of available passive and active functionalities. Nevertheless, typical device footprints are limited by diffraction to several hundreds of micrometers, which hinders emerging nanoscale applications at terahertz frequencies. While metallic gap modes provide nanoscale terahertz confinement, efficiently coupling to them is difficult. Here, we present and experimentally demonstrate a strategy for efficiently interfacing subterahertz radiation (λ = 1 mm) to a waveguide formed by a nanogap, etched in a gold film, that is 200 nm (λ/5000) wide and up to 4.5 mm long. The design principle relies on phase matching dielectric and nanogap waveguide modes, resulting in efficient directional coupling between them when they are placed side-by-side. Broadband far-field terahertz transmission experiments through the dielectric waveguide reveal a transmission dip near the designed wavelength due to resonant coupling. Near-field measurements on the surface of the gold layer confirm that such a dip is accompanied by a transfer of power to the nanogap, with an estimated coupling efficiency of ∼10%. Our approach efficiently interfaces millimeter waves with nanoscale waveguides in a tailored and controllable manner, with important implications for on-chip nanospectroscopy, telecommunications, and quantum technologies.**

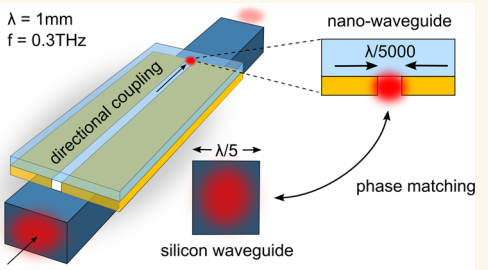

KEYWORDS: *nanophotonics, terahertz photonics, near-field imaging, terahertz time domain spectroscopy, plasmonics*

INTRODUCTION

Terahertz radiation encompasses frequencies in the 0.1−10 THz range, corresponding to wavelengths of 3−0.03 mm, and is increasingly harnessed for numerous far-reaching cross-disciplinary applications. Examples include biosensing[1,2] and spectroscopy,[3] as well as space[4] and ground[5] wireless communication. Historically, the development of efficient terahertz sources has been hindered by fundamental limitations that make both electrically driven and optically inspired approaches inefficient.[6] Nevertheless, recent decades have been marked by rapid technological progress, and the overall consensus is that the terahertz gap is rapidly being bridged.[7]

As terahertz sources and detectors have become increasingly available, the focus has thus started to shift to developing practical devices and experimental techniques for harnessing terahertz radiation effectively. On the one hand, it is important to develop unified and reliable protocols to aid reproducibility in the context of biospectroscopy;[1] on the other hand, it is becoming increasingly important to access a library of chip-scale integrated components that can manipulate terahertz radiation without using bulky free space optics.[8,9] Indeed, a plethora of applications can be realized when terahertz frequencies and nanotechnology converge, particularly in biological analysis, electronic and photonic devices, imaging, spectroscopy, and sensing.[10] For example, nanoscale and macroscale properties can differ significantly,[11,12] warranting practical and reliable platforms to study such regimes. In this context, the fundamental challenge is that the wavelength of terahertz radiation is at least 3 orders of magnitude larger than those needed in the realms of nanotechnology. With conventional techniques, addressing individual nanostructures terahertz at frequencies is impossible due to the diffraction limit;[13] this can be overcome with terahertz scanning near-field optical microscopy, which can achieve microscale resolution over large areas,[14,15] and nanoscale resolution (i.e., nanoscopy[16]) over smaller areas,[17] even in aqueous environments.[18] Terahertz nanotechnology has also benefited from the development of increasingly efficient terahertz sources,[19,20] detectors,[21] and modulators,[22] by enhancing light−matter interactions in small volumes. We point the reader to refs 11,16 and references therein for an overview of terahertz nanotechnology.

Received: July 14, 2024
Revised: October 7, 2024
Accepted: October 10, 2024
Published: October 21, 2024

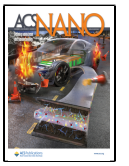

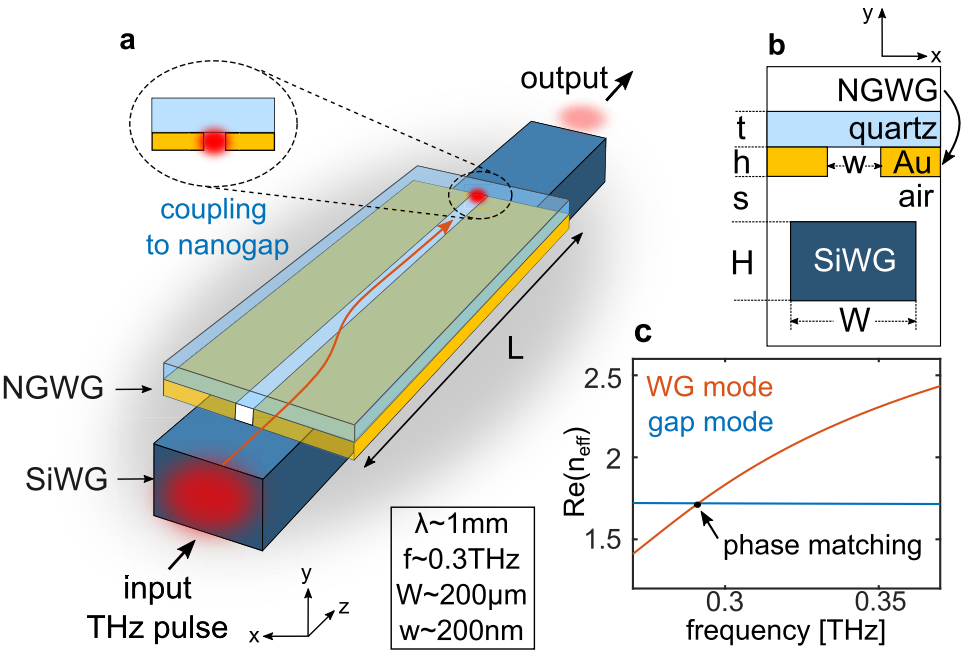

Figure 1. Concept schematic of the terahertz directional nanocoupler presented here. (a) An *x*-polarized broadband terahertz pulse propagates in *z* through a substrateless silicon waveguide (SiWG). At $\lambda \sim 1$ mm, it efficiently couples to the metallic gap mode over a length *L*, due to phase matching with the fundamental mode of the nanogap waveguide (NGWG) above it. (b) Cross section schematic of the coupling region in the *xy* plane, showing geometry and material distribution (light blue: quartz; dark blue: silicon; yellow: gold; white: air). Here, $t = 50\ \mu$m, $h = 100$ nm, $H = 250\ \mu$m, $W = 190\ \mu$m, $w = 200$ nm, and *s* is varied. Note that the schematic is not to scale to simplify labeling and that waveguide and gap widths differ by 3 orders of magnitude: $w \sim \lambda/5000$. (c) Calculated dispersion of $\Re e(n_{\mathrm{eff}})$ of the fundamental modes of the individual SiWG (red) and NGWG (blue), as a function of frequency, highlighting the phase matching point near 0.3 THz.

In parallel, there has been growing interest in developing a general-purpose integrated terahertz platform. For example, in ref 23, Headland et al. argue that all-silicon substrateless waveguides—whose cross section is of order $200 \times 200\ \mu$m^2, and whose length is of the order of the centimeters—are one of the more promising candidates, because of their intrinsic compactness, ease-of-design, and wide variety of accessible functionalities. Nevertheless, the lateral field confinement in such platforms is intrinsically limited by diffraction to $\sim$100 μm at terahertz frequencies, hindering nanoscale applications. The only practical way to confine radiation to deep subwavelength scales is by using metallic components[24] which, in the simplest configuration, can be assembled into a nanomirror cavity that confines linearly polarized radiation inside a nanogap, giving rise to a nanoscale-bound and propagating terahertz mode.[25] This is commonly referred to as the metal/dielectric/metal (MDM) configuration although similar properties can be achieved by nanowires using radial polarization.[26] This confinement is typically accompanied by Ohmic losses, which constitute an important limitation to practical applications.[25] In addition, the small mode area makes direct coupling to such modes from free space challenging. At terahertz frequencies, this problem is further exacerbated by the enormous difference in size and field distribution between dielectric and MDM modes, which in the present context requires a millimeter-to-nanometer mode converter. As a result, most integrated optical-to-terahertz generation and detection schemes use the chip component to support optical waveguiding, which in turn interfaces with external (free space) terahertz fields[27]—we refer to refs 28,29 for recent reviews of hybrid integrated terahertz photonic devices. Furthermore, most schemes that use metallic nanogaps, e.g., for sensing[30−32] or terahertz detection,[33] do so in a planar (metasurface) configuration of deep subwavelength thickness and under free space illumination that is perpendicular to the surface,[34] with an intrinsically small overlap between the incoming diffraction-limited terahertz beam and the nanoscale gaps. In contrast, this work considers the case where the direction of propagation in *z* is parallel to the surface so that the nanogap acts as a waveguide.

In order to achieve an all-integrated platform where *both* optical and terahertz signals propagate on a photonic chip over wavelength scales, it is first necessary to efficiently transfer power from a guided-wave terahertz signal to an area of $\sim 200 \times 200$ nm^2, comparable to that of typical photonic waveguides. The most direct approach is arguably end-fire coupling from the gap waveguide edge;[35] however, in the present configuration, the huge mismatch between the guided mode and a diffraction-limited free space beam leads to low coupling efficiencies. Another approach adapted at near-infrared frequencies, which is also suited for photonic integration, is directional or adiabatic coupling,[36] whose underlying formalism relies on matching the propagation constants of two adjacent modes,[37] and is agnostic to the physical dimensions of the waveguides. Most recently, for example, a millimeter-wave mode converter has been shown to efficiently transfer signals from a silicon waveguide to an antenna of $\sim$10 μm lateral dimensions placed directly on top.[38] More broadly, several nanoscale mode converters on the basis of directional[39] and adiabatic[40] coupling have been developed in silicon-on-insulator substrates at infrared wavelengths. The principle of operation relies on the fact that the effective index of nanoscale metal waveguides (e.g., metal nanowires or nanogaps) can be significantly above that of the surrounding medium when the waveguide dimensions are comparable to the skin depth of the metal at that frequency.[41,42] Therefore, even metal

https://doi.org/10.1021/acsnano.4c09434
ACS Nano 2024, 18, 30626−30637

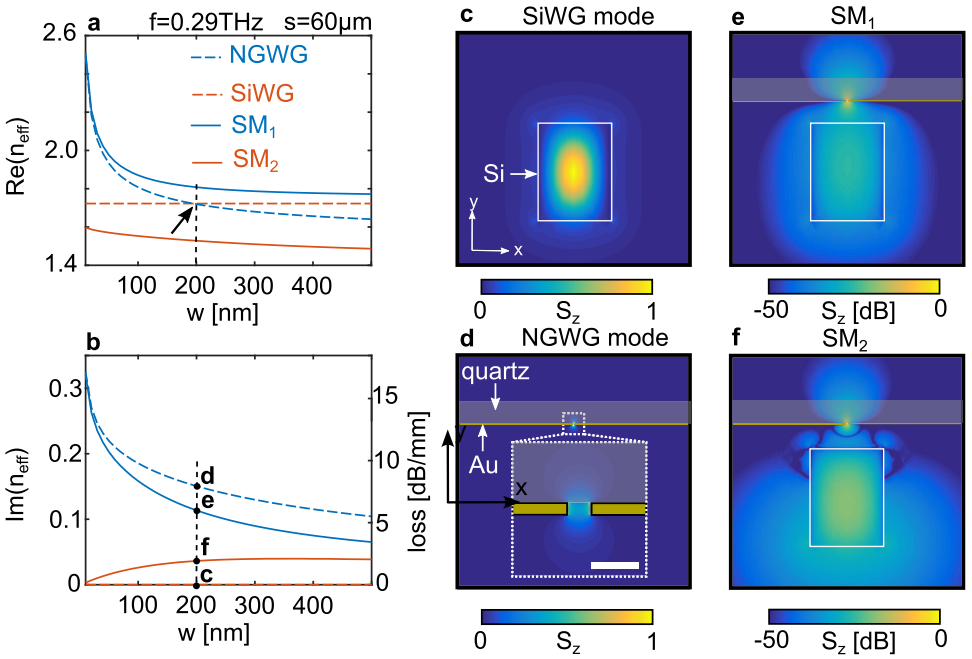

Figure 2. (a) Real part of the effective index of relevant modes as a function of the gap width w, at $f = 0.29$ THz and $s = 60\ \mu$m, with all other parameters as per Figure 1 caption. The dielectric WG (SiWG) remains unchanged with w (red dashed line). The effective index of the nanogap mode increases with decreasing w (blue dashed line), and the phase matches with the WG mode at $w = 200$ nm. The modes hybridize when the waveguides are adjacent, resulting in two supermodes (SMs, solid lines), whose effective indices split at the phase-matching point. (b) Corresponding imaginary part of the effective index. (c, d) Colormap of the WG and gap modes (z-component of the Poynting vector), with a detail of the white dashed region in the inset of (d). (e, f) Hybrid SM_1 and SM_2 that emerge when the waveguides couple, respectively. A logarithmic scale is used due to the large relative field intensity in the nanogap. Window size in (c)−(f): 600 μm × 600 μm. Scale bar in (d) inset: 400 nm.

waveguides in air can be phase-matched with high-index dielectric waveguides; at terahertz frequencies, the skin depth of most metals is ∼100 nm,[43] which immediately suggests the potential for phase matching between nanometer metal waveguides and wavelength-scale dielectric waveguides.

A concept schematic of the device layout and operating principles is shown in Figure 1(a). The device is composed of a millimeter-scale silicon waveguide (SiWG) which is adjacent to a metallic nanogap waveguide (NGWG), and whose lateral dimensions differ by 3 orders of magnitude. The NGWG rests on a quartz substrate with length $L = 3.7$−4.5 mm. The input is a broadband terahertz pulse (frequency: 0.2−3 THz) propagating in the silicon waveguide as per Figure 1(a). Note that both the SiWG and the NGWG substrate are suspended in air and that they can be easily and independently handled with micrometer stages. A schematic of the cross section of the device is shown in Figure 1(b). The SiWG has a height $H = 250\ \mu$m and width $W = 190\ \mu$m; the NGWG has a width $w = 200$ nm and height $h = 100$ nm, supported by a quartz substrate of thickness $t = 50\ \mu$m. The edge-to-edge separation between the waveguides is s, which here lies in the range 10−150 μm.

We first consider the two waveguides separately (i.e., assuming $s = \infty$). The calculated dispersion of the real part of the effective index n_{eff} of the fundamental x-polarized suspended SiWG mode is shown as a red line in Figure 1(c), assuming a constant refractive index of 3.42 for silicon[44] and neglecting losses for simplicity. Note the rise in effective index with frequency due to an increase in the fraction of the mode field in high-index silicon. The corresponding $\Re e(n_{\mathrm{eff}})$ of the NGWG mode is shown as a blue line, which is nominally independent of frequency in this range, considering a lossless refractive index of 2.09 for quartz[45] and taking a Drude−Lorentz model for gold.[46] Under these conditions, the SiWG and NGWG modes phase match at 0.29 THz and are expected to couple as they are brought closer, leading to the emergence of two supermodes that produce efficient power transfer between waveguides via directional coupling. We now discuss this in more detail for the present geometry.

RESULTS

Before discussing the power transfer from the SiWG to the NGWG, we first consider the modes supported by the coupled waveguides during propagation along the device length L as per Figure 1. The most intriguing aspect to analyze, in the first instance, is how the phase matching between the SiWG and the NGWG emerges and how this leads to mode hybridization. The blue dashed lines in Figure 2(a),(b) show the result of two-dimensional (2D) finite element method (FEM) simulations with a commercial tool (COMSOL Multiphysics) of the real- and imaginary- parts of the effective index of the fundamental mode of the isolated NGWG as a function of w at a constant frequency of 0.29 THz—see the Methods section for details of the simulation and material parameters used. Note in Figure 2(a) the sharp increase in both real and imaginary parts of n_{eff} as w is decreased, with n_{eff} approaching the effective index of the quartz slab mode as w increases. The right axis of Figure 2(b) plots the associated loss, which is 5 dB/mm, indicating that the millimeter-scale propagation of this NGWG mode is supported. The x-polarized mode effective index of the isolated SiWG is fixed (being w independent), purely real (i.e., lossless), and marked by the horizontal red dashed line in Figure 2(a). The Poynting vector associated with this mode is shown in Figure

https://doi.org/10.1021/acsnano.4c09434
ACS Nano 2024, 18, 30626−30637

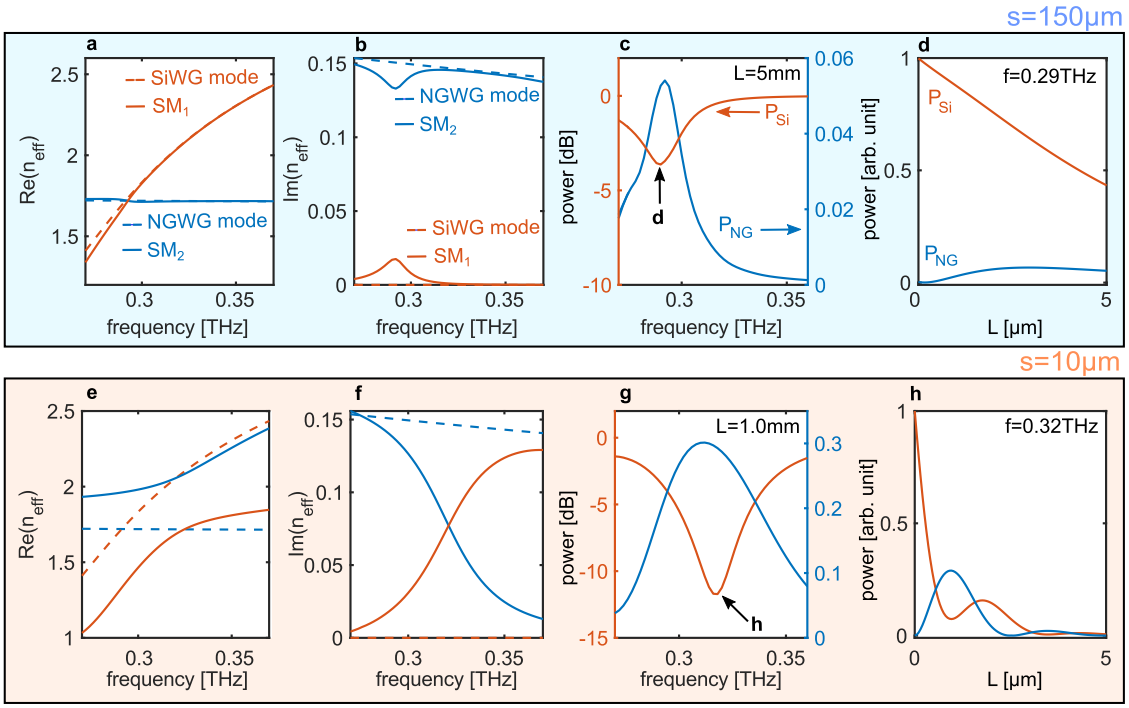

Figure 3. Overview of the effective index dispersion, transmission spectra, and power exchange properties for different separations *s*. (a) For larger separations (s = 150 μm, blue box), the real part of the effective index for both isolated and coupled WG/gap modes cross, and (b) the imaginary parts anticross. (c) Associated calculated power in the dielectric waveguide P_{Si} as a function of frequency for L = 5 mm (red line, left axis on dB scale), showing resonant transmission dip accompanied by a corresponding transmission peak in the nanogap waveguide power P_{NG} (blue line, right axis). At the resonance frequency (0.29 THz, black arrow), (d) shows that the P_{Si} monotonically decreases with increasing length L, with P_{NG} plateauing at ∼0.05, decreasing at longer lengths due to losses. Bringing the waveguides closer (s = 10 μm, green box) leads to (e) an anticrossing in the real parts of the SM dispersions, (f) and a crossing of their imaginary parts, due to stronger coupling.[37] (g) The resulting transmission dip is sharper for shorter device lengths (here: L = 1.0 mm) due to directional coupling (red lines, left axis). Correspondingly, more power is coupled to the plasmonic gap. Note that the P_{Si} minimum has shifted to 0.32 THz (black arrow in (g)). (h) At this frequency, the power in the SiWG oscillates and decays (red line), whereas the relative power in the NGWG peaks at $L \sim 1.0$ mm.

2(c), whereas that of the isolated NGWG mode is shown in Figure 2(d). Note that the latter possesses a vastly reduced mode volume compared with the SiWG mode. A zoomed-in view of this mode is shown in the inset of Figure 2(d) for w = 200 nm. If the two waveguides are placed side by side (e.g., s = 60 μm), then the modes hybridize, giving rise to so-called supermodes (SMs), which constitute the modes of the two-waveguide system. According to coupled mode theory, under the weak coupling approximation, SMs are even- and odd- superpositions of the isolated modes at the phase matching point.[47] Here, the modes are strongly coupled, and their propagation constants and field distributions must be calculated numerically. The solid lines in Figure 2(a),(b), respectively, show the real and imaginary parts of the effective index of the SMs as a function of w at 0.29 THz. Note that $\Re e(n_{eff})$ now anticross at the phase matching point and that both modes are lossy (i.e., $\Im m(n_{eff}) > 0$ for both SMs). The colormaps of the associated SMs for w = 200 nm (Figure 2(e),(f), respectively), clearly show modal hybridization.

Because the propagation constants of the participating isolated modes are complex valued, the coupler is non-Hermitian,[48] and the resulting mode hybridization subtly depends on the interplay of coupling strength and loss—see, for example, ref 49 for a review of non-Hermitian photonics, and ref 50 for a non-Hermitian perspective on plasmonic couplers. For ease of discussion, here we only consider how the SMs of the two-waveguide system depend on frequency and separation, and device length in the present context, which we will subsequently experimentally access, and how this is expected to influence the transmission through the dielectric waveguide and the associated power transfer to the NGWG.

Simulations. We are predominantly interested in the understanding of how energy is transferred between the dielectric and the metal gap waveguide under different configurations. Most commonly,[51] complex coupler designs are understood and optimized via three-dimensional full-field numerical modeling, e.g., using finite element, or finite-difference time domain methods. However, such approaches are not practical in the present case, because the size of the gap is more than 3 orders of magnitude smaller than the propagation length, making memory requirements and calculation times prohibitive for full three-dimensional models.[37] Instead, we use the eigenmode expansion method, which relies on a combination of two-dimensional mode numerical calculations and analytical formulas[37,52] for propagation in z—see the Methods section for further details. We now discuss a few representative cases that elucidate the expected coupling between the waveguides under different conditions.

We consider all relevant eigenmodes as a function of frequency f and separation s, taking w = 200 nm, and all other parameters as in Figure 2. The top row of Figure 3 shows a summary of the case where s = 150 μm, i.e., at $\sim \lambda/6$ distance between the SiWG and the NGWG. Figure 3(a),(b) details the real and imaginary parts of the isolated modes and SM dispersion, using the same notation as in Figure 2. The isolated modes phase match, as per our plot in Figure 1(c); however, contrary to our analysis in Figure 2, Figure 3(a) shows that the

https://doi.org/10.1021/acsnano.4c09434
ACS Nano 2024, 18, 30626−30637

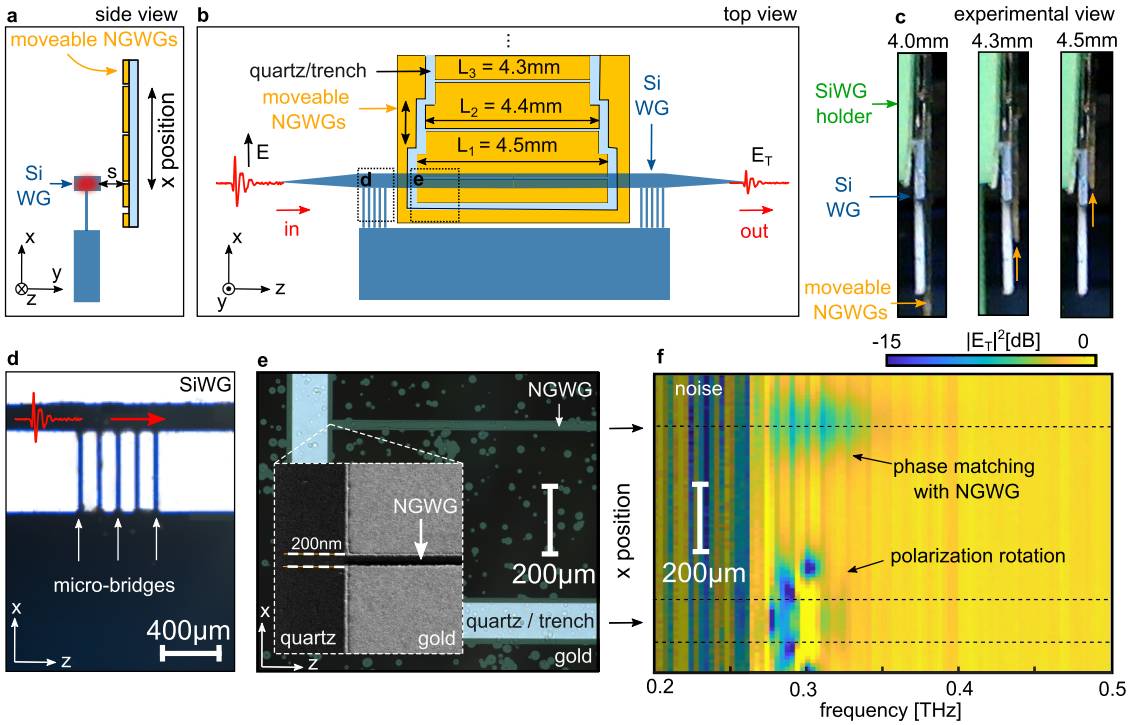

Figure 4. Summary of the far-field transmission experiments. (a) Side view of the experiments. An *x*-polarized THz pulse (red) is coupled to the fundamental mode of the substrateless silicon waveguide (SiWG, dark blue). A series of metal nanogap waveguides (yellow) on a quartz substrate (light blue) are moved in *x* for a given separation *s*. (b) Top view of the experiment. The NGWGs vary in length (here: L = 3.7−4.5 mm). We measured the transmitted intensity $|E_T|^2$ of the THz pulse through the SiWG as a function of *x*. (c) Microscope images of the experiment for different values of L as labeled. The green is a custom holder for the SiWG. Note the moving NGWGs for a fixed input condition. (d) Optical micrograph of the SiWG and microbridges. (e) Optical micrograph of the gold NGWGs deposited on quartz surrounded by a 100 μm trench, included to facilitate visual inspection. Inset: scanning electron micrograph of the NGWG edge, showing the 200 nm gap. (f) Measured colormap of the transmitted intensity through the SiWG as a function of frequency and the *x*-position of the NGWG sample for a constant $s \sim 50$ μm, covering both the trench and the 4.5 mm NGWG sample.

real parts of the SM effective indexes cross, precluding directional coupling, since the coupling length at the phase matching point, $L_c = \lambda/\Delta n_{\text{eff}}$, turns out to be infinite.[53] This takes place because at the considered separation distance ($s \sim \lambda/6$), the coupling is too weak to produce eigenmode splitting.[37] Although these waveguides are very close ($s < \lambda/5$), the NGWG mode is confined close to the nanofilm (inset in Figure 2(d)), and the effective index's imaginary part is relatively large (~10% of its real part), precluding the SMs' avoided crossing. The associated $\Im m(n_{\text{eff}})$, shown in Figure 3(b), anticross. As expected,[53] the loss of SM_1 increases near the phase matching point which, in turn, produces a drop in the overall transmission because in this regime the fundamental mode of the incoming waveguide predominantly couples to SM_1.[50] To confirm this, we calculate the normalized power in the dielectric waveguide P_{Si} as a function of frequency for L = 5 mm which is shown on a dB scale in Figure 3(c) (red line, left axis), and presents a broad transmission dip at 0.29 THz. The corresponding calculated normalized power in the nanogap waveguide P_{NG} is shown on a linear scale in Figure 3(c) (blue line, right axis). We find that more than 5% of the incoming power is predicted to couple to the nanogap despite having a lateral dimension of less than $\lambda/5000$. Phase matching, even at relatively large distances and without achieving eigenmode splitting, can be harnessed to access nanoscale mode areas from dielectric waveguides with percentage-level efficiency. Figure 3(d) shows P_{Si} and P_{NG} at 0.29 THz resonance as a function of L. Note that the power in the SiWG monotonically decreases with L, whereas the power in the NGWG reaches a plateau due to losses.

When the waveguides are brought closer and their modes couple more strongly, the power exchange properties of the nanocoupler are significantly modified. The bottom row of Figure 3 shows the plots corresponding to the top row but now taking s = 10 μm. The solid lines in Figure 3(e),(f), respectively, show the real and imaginary parts of the SM dispersions. The coupling is now strong enough to produce eigenmode splitting,[37] and the real parts of the effective indices of the SMs anticross, while their imaginary parts cross. Note that the frequency of the SM anticrossing point in Figure 3(e) (i.e., where the difference in their $\Re e(n_{\text{eff}})$ is minimum) occurs at a higher frequency than the phase matching point. In this case, an accurate computation of the transmission spectra must take into account each mode's excitation and propagation along the device length L via eigenmode expansion method[52] (see the Methodssection). The calculated P_{Si} as a function of frequency for L = 1 μm is shown on a dB scale in Figure 3(g) (red line, left axis). Compared to the situation at larger separation (cf. Figure 3(c)), the transmission dip shifts to a higher frequency of 0.32 THz. Furthermore, as a result of the short device length and the possibility of resonant interference between modes due to a splitting of the eigenmodes, the associated normalized P_{NG} increases to 0.3, peaking when P_{Si} is at a minimum as shown in Figure 3(h) (blue line, right axis). Figure 3(h) shows P_{Si} and P_{NG} at 0.32 THz, showing lossy oscillatory behavior with

https://doi.org/10.1021/acsnano.4c09434
ACS Nano 2024, 18, 30626−30637

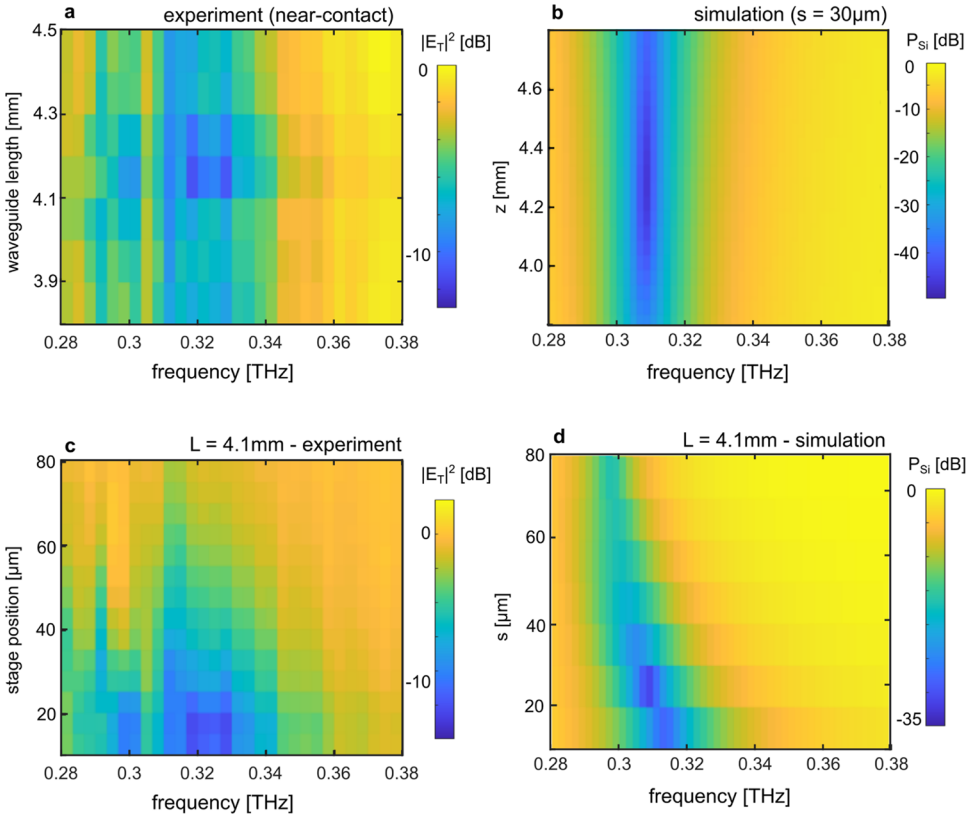

Figure 5. Dependence of the nanocoupler transmission on the length L of the NGWG and separation s to the SiWG. (a) Measured transmitted intensity spectrum when the SiWG and NGWG are in near-contact, as shown in Figure 4(c), for different L's. (b) Eigenmode method simulations of the power spectrum in the SiWG when $s = 30\,\mu$m. (c) Measured transmitted intensity spectrum as a function of s for $L = 4.1$ mm. Note the emergence of a resonance as the waveguides are brought closer. (d) Corresponding eigenmode method simulations of the power spectrum in the dielectric waveguide as a function of s.

increasing length, as expected for coupled lossy waveguides in this regime.[37,53]

Far-Field Transmission Experiments. In a first set of experiments, we measure the transmission through a SiWG that is adjacent to a gold film containing a series of NGWGs of varying lengths. Figure 4(a),(b) shows side- and top-view schematics of the sample positioning and experimental setup, respectively. All materials are color-coded as per Figure 1(b). The SiWG layout is inspired by previous designs:[54,55] it is formed by a suspended silicon strand of 1 cm length, which is connected to a silicon substrate (substrate area: 1 cm × 1 cm) via subwavelength microbridges to minimize scattering of the fundamental mode upon propagation. An additional taper on each end of the waveguide (taper length: 1 cm) facilitates coupling to and from free space. The NGWGs have lengths between 3.7 and 4.5 mm. Each NGWG is separated in x by 1 mm. The NGWGs are etched on a 100 nm gold film on a quartz substrate of 50 μm thickness. Each waveguide is surrounded by a trench of width 100 μm to facilitate alignment, highlighted in Figure 4(b). We used a THz time domain spectroscopy (THz-TDS) system to measure the field transmitted by the waveguide. The electric field is polarized in x. Computer-controlled stages enable us to vary both s and the x-position, while the SiWG is kept still after coupling to its fundamental mode.

Figure 4(c) shows an example experimental view obtained from an external microscope when the NGWGs are in near-contact with the SiWG, varying the x-position to align the SiWG with NGWGs of length L as labeled. In detail, Figure 4(d) shows an optical micrograph of the SiWG from the top, highlighting the microbridges and the direction of propagation of the pulse inside the waveguide. Figure 4(e) shows an optical micrograph top view of the NGWGs and trench, which exposes the underlying quartz substrate. We used scanning electron microscopy to confirm that all waveguides considered here are continuous for their entire length. For example, the inset of Figure 4(e) shows the edge of the NGWG. The dark green dots and green bands are areas where chromium (used as an adhesion layer for gold on quartz) was removed during the wet-etching process. In the optical microscope image, obtained via bottom illumination, the isotropically etched chromium underlayer is visible. However, in the SEM image, these features are not seen because the secondary electrons are captured only from the top surface of the gold, giving an accurate representation of the waveguide's true width (200 nm). Note that the NGWG is too small to be sharply resolved under an optical microscope.

To confirm that the SiWG mode is coupling to the NGWG mode, we first measure the terahertz pulse transmitted by the SiWG when it is adjacent to the gold/quartz substrate as a function of the x-position, varying x over the region bounded by the micrograph of Figure 4(e). Our experiment directly measures the terahertz pulse field emerging from the SiWG so that its Fourier transform provides the transmitted amplitude and phase of the electric field at every frequency.[56] Figure 4(f) shows a false color plot of the resulting transmitted intensity as a function of frequency and x-position, where $s \sim 50\,\mu$m is kept constant. Note that we have aligned Figure 4(e),(f) in x for better comparison, i.e., the vertical scale bars coincide. The

https://doi.org/10.1021/acsnano.4c09434
ACS Nano 2024, 18, 30626−30637

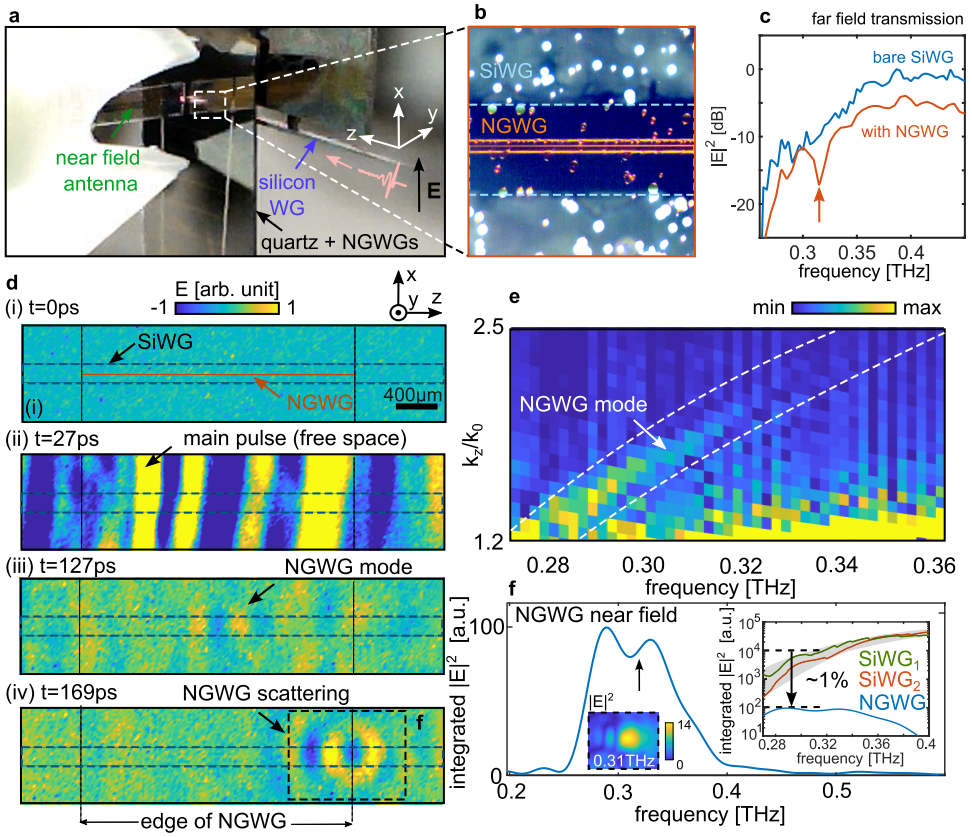

Figure 6. Experimental demonstration of terahertz radiation coupling to a $\lambda/5000$ nanogap waveguide. (a) Microscope image of a terahertz near-field (NF) antenna scanning the surface of a quartz substrate supporting the NGWGs, aligned with a SiWG. Note that the incoming electric field is *x*-polarized and that the NF antenna detects *x*-polarized fields. (b) Optical micrograph of the substrate, highlighting that the nanogap waveguide is in the center of the SiWG. The spots are residuals from the fabrication process and represent minor surface contaminations that do not provide additional scattering; see Animation 1 in the Supporting Information. (c) Far-field transmission: the red trace shows the transmitted $|E|^2$ (i.e., the far-field transmission) through the silicon WG for the sample configuration shown in (a) and (b). Note the resonance at 0.31 THz, which is absent for the bare SiWG (blue trace). (d) Snapshots of the measured electric field at (i) $t = 0$ ps (no field). The horizontal lines mark the nominal SiWG boundary. The vertical dashed lines highlight the edges of the NGWG ($L = 4.4$ mm). The orange horizontal line shows the nominal location of the NGWG, as per (b). (ii) Field snapshot at $t = 27$ ps (main pulse is from the scattered field that does not couple to the SiWG), (iii) $t = 127$ ps (evanescent field of the NGWG mode), and (iv) $t = 169$ ps (field scattered by the end of the NGWG). The complete animation showing pulse propagation is reported in Animation 1 in the Supporting Information. (e) Measured dispersion of the detected NGWG mode using the data in (d)(iii). (f) Measured distribution of the scattered electric field intensity at the end of the NGWG using the data in (d)(iv). The scattered intensity is centered at 0.31 THz, confirming that the dip in (c) is due to coupling to the nanogap. Inset: comparison of the measured total intensity scattered by the nanogap (dashed box in (d)(iv)) and the estimated intensity exiting the SiWG from two independent measurements, showing percentage-level coupling efficiency. Also shown below the curve is an example of measured intensity scattered by the nanogap following a temporally gated Fourier transform for the case of 0.31 THz.

dashed lines in Figure 4(f) overlap with the edge of the trench and the center of the NGWG. We observe a series of sharp transmission dips near 0.3 THz as we move the trench over the SiWG. Our 3D finite element calculations suggest that these dips are due to polarization rotation[57,58]—see Figure S1 in the Supporting Information—which we measure because the detector records *x*-polarized fields. Analogous polarization rotation effects using gold nanostrips over a silicon waveguide have been studied in the near-infrared.[59] A detailed discussion is beyond the scope of this work; nevertheless, such resonances provide a useful marker for discerning the resonance due to phase matching between the SiWG and the NGWG, which appears near 0.3 THz when the longest NGWG passes over SiWG. Note that the signal below 0.26 THz is independent of the *x*-position, but close to the noise floor, because the fundamental mode of the SiWG approaches the light line (solid red line in Figure 3(a)).

This first experiment indicates that resonant coupling to the NGWG mode is occurring. We now proceed with a more detailed analysis, accounting for both changes in NGWG length L and separation s from the edge of the SiWG. According to Figure 3(h), in near-contact ($s = 10$ μm), we expect to measure an oscillation of the power transmitted by the SiWG when changing L. To measure this experimentally, we repeat the transmission experiments through the SiWG, changing the length of the adjacent NGWG. Figure 5(a) shows a false color plot of the measured transmitted intensity as a function of frequency and waveguide length L, where the SiWG and NGWGs are in near-contact for each measurement, and correspond to the micrographs of Figure 4(c). We observe that the resonance depth possesses a minimum for $L = 4.1$ mm, and increases both for longer and shorter NGWG lengths, confirming the expected oscillatory behavior (see, for example, red line in Figure 3(h)). Figure 5(b) shows a simulation of P_{WG} for $s = 30$ μm, i.e., the power contained in the SiWG, showing

https://doi.org/10.1021/acsnano.4c09434
ACS Nano 2024, 18, 30626−30637

good overall qualitative agreement with the measurements (cf. Figure 5(a)). By considering the L = 4.1 mm NGWG, and increasing the stage position, notice the expected gradual weakening and red-shifting of the resonance, as detailed in Figure 5(c), as per the results of Figure 3 (see the dip in the red traces of Figure 3(c),(g)). Figure 5(d) shows the corresponding simulated P_{WG} as a function of s for L = 4.1 mm, again showing good agreement with the measurements (Figure 5(c)).

Near-Field Experiments. The above experiments confirm that the terahertz field at frequencies near 0.3 THz is coupled out of the SiWG if it is adjacent to the NGWG. In a final set of experiments, we wish to confirm that such fields are indeed propagating inside the nanogap. We therefore modify the experimental setup to enable measurement of the evanescent field, associated with the NGWG mode, via a near-field terahertz antenna.[15,60] A photograph of the experimental setup is shown in Figure 6(a), including the reference frame (white), direction of propagation (red), and field polarization (black). Figure 6(b) is a top-view micrograph detail of the sample configuration, showing that the NGWG (yellow) is centered over the SiWG (dark region, bound by the blue dashed lines). This was achieved using a laboratory microscope and manual alignment with a standard translation stage, followed by gluing. Once aligned and bonded, the device becomes monolithic, and no further alignment is needed. This configuration allows a far-field transmission measurement through the SiWG in first instance, followed by a near-field measurement of the electric field above the sample in second instance. The red trace in Figure 6(c) represents the field intensity spectrum transmitted through the SiWG in this configuration and reveals, in a clear-cut way, a resonance dip relative to the bare SiWG case (blue trace).

Figure 6(d) shows representative snapshots of the measured electric field distributions at different time intervals. For clarity, panel (i) shows the SiWG boundaries as horizontal lines, whereas the vertical dashed lines highlight the edges of the NGWG (L = 4.4 mm). The orange horizontal line shows the nominal location of the NGWG. The first signal to appear, at t = 27 ps, is associated with the portion of the incoming pulse that does not couple to the silicon waveguide and scatters around it, as shown in Figure 6(d)(ii). At a later time, a pulse confined to the middle of the scanning window appears, shown in Figure 6(d)(iii) for t = 127 ps, corresponding to the location of the NGWG. We attribute this signal to the evanescent field above the quartz substrate, associated with the NGWG mode, coupled to the SiWG mode. Figure S2 in the Supporting Information compares the relevant calculated mode profiles with and without the nanogap: in the absence of a nanogap, no measurable field would be present in this location. These fields move more slowly than the free space pulse, due to the larger group velocity associated with the NGWG. Once this pulse reaches the end of the NGWG, we observe the emergence of a point-dipole-like emission pattern, shown in Figure 6(d)(iv) for t = 169 ps, confirming that a significant portion of the field was indeed coupled to and propagating inside the nanogap, before being scattered in the y direction once the NGWG terminates. The complete and annotated animation associated with Figure 6(d) and the surrounding text is shown in Animation 1 in the Supporting Information.

Because THz-TDS measures the electric field of the terahertz pulse, including amplitude and phase information, we can obtain the frequency-dependent amplitude and phase in the xz plane from a temporal Fourier transform. An example of the amplitude and phase map retrieved at 0.29 THz is shown in Figure S3 in the Supporting Information. In turn, a spatial Fourier transform of the complex field $\tilde{E}(k_z, k_x)$ can be used to obtain information on the distribution of the participating modes. For example, $|\tilde{E}(k_z, k_x)|$ at 0.29 THz is shown in Figure S3(b). Two salient spatial modes can be distinguished close to the phase-matching frequency of 0.3 THz: the first is near $(k_z/k_0, k_x/k_0) = (1, 0)$, corresponding the main pulse of Figure 6(d)(ii), which propagates in free space; the second is near $(k_z/k_0, k_x/k_0) = (1.6, 0)$, corresponding to the later pulse propagating in the NGWG, shown in Figure 6(d)(iii). We can confirm that this is the NGWG mode by applying a band-pass filter around the NGWG in $k_z/k_0 = 1.6 \pm 0.2$ and performing an inverse spatial Fourier transform. The associated field amplitude is shown in Figure S3(c), ascertaining that the field is centered in the waveguide. By binning the contribution of all k_x values (i.e., by summing all rows in Figure S3(b)) at each temporal frequency, we obtain a colormap of the mode dispersion. The result is shown in Figure 6(e): we note the excitation and detection of modes with propagation constants above unity—bounded by the white dashed lines—follow the dispersion of the underlying dielectric waveguide mode (see also Figure S4 in the Supporting Information). This overlap between the dispersions of the propagating modes measured above the nanogap and below the dielectric is an indication of coupling between the two waveguides.

We consider this effect in more detail by quantifying the field scattered by the NGWG endface once the pulse reaches the end of the NGWG, corresponding to the event shown in Figure 6(d)(iv). First, we temporally gate the data so that only the scattering event is captured (here: between 161 and 190 ps). Second, we take a temporal Fourier transform and thus obtain the field intensity $|E|^2$ at each frequency. Because the field propagates in y (i.e., perpendicular to the xz plane) and in free space, we estimate the total power as the integral of $|E|^2$ over the 2 mm × 1 mm window centered in the scattering source (black dashed rectangle in Figure 6(d)(iv)). An example of the scattered intensity distribution at 0.31 THz is shown in the lower inset of Figure 6(f). The resulting integrated $|E|^2$ as a function of frequency is shown in Figure 6(f), indicating that its distribution peaks near 0.31 THz, coinciding with the dielectric waveguide resonance in Figure 6(c). This experimentally confirms that coupling from the SiWG to the NGWG has occurred.

Finally, we estimate the order of magnitude of the coupling efficiency from the SiWG to the nanogap. We consider the integral of the modulus squared of the field exiting the SiWG at the output, measured by the near-field antenna in this configuration, to obtain the estimated power propagating in z and exiting the silicon waveguide. Our method uses the field distribution near the output taper of the SiWG in the xz plane to estimate the field intensity propagating in z in the xy plane at each frequency—see Figure S5 in the Supporting Information and associated text for additional information. The resulting estimated integrated intensity exiting the SiWG is shown in the inset of Figure 6(f) as red and green lines for two independent measurements and plotted on a logarithmic scale. A comparison with the integrated intensity scattered by the nanogap (blue line), suggests that the coupling efficiency is at least of the order of ~1% with respect to the power inside the silicon waveguide. Note that this ratio considers only the measured power scattered by the nanogap which, owing to the deep subwavelength nature of the nanogap, does not emit efficiently into free space. Calculations in COMSOL suggest that the power in the nanogap itself is at least 10 times higher than the one emitted

https://doi.org/10.1021/acsnano.4c09434
ACS Nano 2024, 18, 30626−30637

out-of-plane, indicating that the coupling efficiency from the SiWG to the NGWG is in fact at least 10%—see Figure S6 and associated text in the Supporting Information. Indeed, the simulations in Figure 3(g) indicate that the coupling efficiency could be as high as 30%. Verifying this claim, however, would require the use of terahertz scanning near-field optical microscopy inside the gap itself,[16] which is a significantly more complicated experiment, and is beyond the scope of this work.

We would like to point out that while a coupling efficiency of order 10% may seem low compared to directional coupling schemes between lossless waveguides, it represents a significant achievement, given that coupling occurs between two waveguides with such vastly different cross-sectional areas (area ratio: 0.4×10^{-7}). For example, direct end-fire coupling would yield a coupling efficiency many orders of magnitude less than 10%, due to negligible overlap between the two waveguide modes. Nevertheless, there are potential strategies for improving this efficiency in future iterations of the device. For instance, optimizing the distance between the two waveguides via automated alignment techniques could yield the highest possible coupling efficiency for a given loss. Additionally, tapering or other mode-conversion techniques could be explored to ease the transition between the vastly different mode sizes.[38]

CONCLUSIONS

In summary, we have proposed and experimentally demonstrated a directional nanocoupler capable of bridging millimeter- and nanometer-scale terahertz photonics. Our scheme implements phase matching between a submillimeter dielectric waveguide and sub-μm metal gap waveguides, leading to resonant power transfer between them when they are placed side by side. This approach overcomes significant limitations in terms of coupling efficiency between waveguides that differ by 3 orders of magnitude in lateral dimensions. To demonstrate the effect, we have performed a comprehensive set of complementary experiments near 0.3 THz (i): far-field experiments which measure the transmission through the THz nanocoupler; (ii) near-field experiments which measure the field associated with the nanogap waveguide. In the first set of experiments, we clearly observed the emergence of a resonant dip when the two waveguides are separated by less than 100 μm; in the second set of experiments, we measured the propagation constant and field scattering of the mode inside the nanogap. Overall, the power scattered by the gap waveguide is ~1%, suggesting that the power in the gap itself could be more than 10%, with simulations indicating that this could be as high as 30%. Our results contribute to the development of solutions for photonic integration at terahertz frequencies, potentially impacting several emerging technologies. The tight field confinement provided by our device is particularly relevant for terahertz near-field microscopy, since it allows for the probing of materials and molecules at nanoscale resolutions, making it suitable for applications in biological sensing and molecular fingerprinting. Note in particular that the scattered signal shown in Figure 6(iv) originates from the nanochannel alone, and thus could potentially be used for retrieving the background-free terahertz phase shift or spectroscopic fingerprint of any element inside the nanochannel (e.g., individual proteins[61]), with implications for on-chip terahertz biosensing.[62] For telecommunication applications, the subwavelength confinement and the potential for operating at terahertz frequencies naturally lends itself to extreme nonlinear interaction between terahertz and optical waves on-chip,[63] in the context of terahertz generation[64] and detection.[27] In turn, this platform would enable a direct interface between millimeter-wave (6G) chips and photonic integrated circuits, with applications in optical-to-terahertz interconnects for increased data transmission speeds, lower power consumption, and reduced device footprint. Moreover, the ability to confine terahertz fields at the nanoscale can potentially boost emerging quantum technologies at terahertz frequencies:[65] our nanogap waveguide can directly interface with quantum emitters, with potential applications in on-chip quantum sensors and quantum communication devices.

With regard to the scalability of this fabrication process, two separate issues need to be considered: (i) waveguide alignment and (ii) fabrication of the nanowaveguides with appropriate dimensions, which here relies on electron-beam lithography. While close proximity between the waveguides is essential for device function, we believe this is not a significant limitation: the waveguides can be placed in near-contact by simply placing one over the other, as we do here; additionally, centering the nanogap waveguide over the entire silicon waveguide was achieved by using a laboratory microscope and manual alignment with a standard translation stage. However, for larger-scale applications, a microscope-based alignment may not be practical. In future devices, this procedure can be implemented via automated alignment systems (e.g., flip-chip bonders), improving scalability and reducing reliance on manual processes. Typical commercial flip-chip bonders have automated alignment accuracies below 1 μm in all three directions—significantly better than the accuracy of our manual alignment approach. With regard to the NGWG dimensions, while electron-beam lithography is suitable for achieving the required 200 nm width, it is not industrially scalable. Alternative techniques, such as nanoimprint lithography, could provide a more scalable solution, allowing high-throughput production over larger areas with comparable precision. Moreover, while gold was used here, using aluminum could be more cost-effective and compatible with industrial-scale processing without significant compromise in performance because metals at terahertz frequencies are good conductors. Wafer-scale processing techniques such as deep-UV lithography and metal dry etching could further enhance scalability while ensuring the required dimensional control. We note that this approach is not limited to the specific nanogap geometry considered here: metal nanowires[26,66] and nanofilms[67] could couple to dielectric waveguides via the same mechanism and will likely lead to similar effects. Finally, it should be noted that the coupling efficiency limit of 10−30% is only due to losses in the metal, which emerge because the mode size approaches the metal's skin depth. Adiabatic approaches would also be hindered by this intrinsic limit. If the imaginary part of the mode effective index in the nanogap waveguide approached zero, the coupling efficiency would also approach 100%. Preliminary calculations indicate that increasing the metal conductivity has the effect of reducing both the coupling length and the modal loss, leading to more efficient and compact devices; conversely, lowering the conductivity increases both coupling length and losses. A higher coupling efficiency could be achieved by using either more conductive metals (e.g., silver) or superconductors below their critical temperature.[25,68] Alternatively, terahertz couplers based on other geometric configurations e.g., dielectric-loaded surface plasmon polariton waveguides,[69] might also provide an approach for nanoscale mode confinement with lower losses.

https://doi.org/10.1021/acsnano.4c09434
ACS Nano 2024, 18, 30626−30637

METHODS

Eigenmode Calculations. The propagation constants β_i, and the electric and magnetic fields ($\mathbf{e}_i$, $\mathbf{h}_i$) of the fundamental mode of each waveguide are calculated using COMSOL (Wave Optics Module, Mode Solver)—example geometry and results are shown in Figure 3. We use a constant refractive index of 3.42 for silicon,[44] 2.09 for quartz,[45] and a frequency-dependent Drude–Lorentz model for gold[46]—see Table S1 in the Supporting Information and associated text for more details of the model used. The total electric and magnetic fields propagating in the coupler device can be written as

$$\mathbf{E}(x, y, z) = a_1\, \mathbf{e}_1(x, y)\, \exp(i\beta_1 z) + a_2\, \mathbf{e}_2(x, y)\, \exp(i\beta_2 z),$$
$$\mathbf{H}(x, y, z) = a_1\, \mathbf{h}_1(x, y)\, \exp(i\beta_1 z) + a_2\, \mathbf{h}_2(x, y)\, \exp(i\beta_2 z), \quad (1)$$

where a_i is the modal complex amplitude which determines the contribution of the i-th eigenmode to the total field, following the appropriate normalization.[37] The complex modal amplitudes are given by

$$a_i = \hat{z} \cdot \int \frac{1}{2}[\mathbf{e}_i(x, y) \times \mathbf{h}_0(x, y)]\, \mathrm{d}x\mathrm{d}y \quad (2)$$

where $\mathbf{h}_0(x, y)$ is the magnetic field of the isolated SiWG mode, corresponding to the total field at $z = 0$. The total power in each waveguide is calculated by splitting the simulation space into two regions, using an artificial boundary halfway between the two waveguides at $y_b = s/2$, taking the reference frame as in Figure 1(b) with the origin at the top surface of the SiWG. We define

$$p_{\mathrm{Si}}(z) = \int_{-\infty}^{+\infty} \int_{-\infty}^{s/2} S_z(x, y)\, \mathrm{d}x\mathrm{d}y,$$
$$p_{\mathrm{NG}}(z) = \int_{-\infty}^{+\infty} \int_{s/2}^{\infty} S_z(x, y)\, \mathrm{d}x\mathrm{d}y, \quad (3)$$

where $p_1(z)$ and $p_2(z)$ are the total powers (per unit length) in the SiWG and NGWG, respectively, and where S_z is the z-component of the Poynting vector of the total field. The fraction of power in each region p_1 and p_2, respectively, as a function of propagation length, is thus defined as follows:

$$P_{\mathrm{Si}}(z) = p_{\mathrm{Si}}(z)/[p_{\mathrm{Si}}(0) + p_{\mathrm{NG}}(0)],$$
$$P_{\mathrm{NG}}(z) = p_{\mathrm{NG}}(z)/[p_{\mathrm{Si}}(0) + p_{\mathrm{NG}}(0)] \quad (4)$$

so that $P_{\mathrm{Si}}(0) + P_{\mathrm{NG}}(0) = 1$. Note that, in order to resolve the field in both the NGWG and the SiWG, two integration windows are appropriately interlaced: the SiWG window is 2 mm × 2 mm with a 1 μm pixel; the NGWG window is 4 μm × 4 μm with a 2 nm pixel.

Sample Fabrication. The SiWGs are fabricated by standard photolithography and deep-reactive ion etching[70] on 250 μm high-resistivity float-zone silicon wafers. The NGWG fabrication process is as follows. A quartz substrate (thickness: 150 μm) is piranha cleaned to remove organic contaminants; a 20 nm layer of chromium is deposited by using electron-beam evaporation. The wafer is dipped in Surpass 4000 (DisChem Inc) for 60 s, followed by DI water for 30 s to improve the resist adhesion. ma-N 2403 photoresist (Microresist GmbH) is spin-coated onto the substrate at 3000 rpm, followed by baking at 90 °C for 60 s (film thickness: 275 nm). The NGWGs are patterned via electron-beam lithography (Raith EBPG5150, 100 kV, 550 μC/cm at 1 nA/100 nA with 1 mm write field, 2.5 nm/20 nm beam step for fine and coarse structures). The exposed photoresist is developed in AZ726 for 60 s, followed by a DI water rinse and N_2 drying. A metal layer consisting of 10 nm chromium and 100 nm gold is deposited, followed by lift-off in dimethyl sulfoxide (DMSO) for 20 min at 45 °C. Chromium etching is carried out using Transene 1020 for 45 s. The etch time is calibrated using a dummy sample to achieve the desired etch depth for 30 nm of chromium to avoid the excess delamination of the gold with Cr overetching.

Far-Field Experiments. We use a commercially available THz-TDS System (Menlo TERAK15), which produces THz emission from biased photoconductive antennas that are pumped by fiber-coupled near-infrared pulses (pulse width: 90 fs; wavelength: 1560 nm). Polymethylpentene (TPX) lenses (Thorlabs TPX50) collimate and focus the beam toward the SiWG. The THz field emerging from the SiWG is sampled as a function of the time delay of a fiber-coupled probe pulse on a photoconductive antenna THz detector. The electric field is polarized in x, using the sample orientation and reference frame shown in Figure 6. To produce the images in Figure 4 and Figure 5, the substrate containing the NGWGs is moved via a microcontroller stage for a fixed SiWG coupling condition.

Near-Field Experiments. The THz field on the surface of the waveguides is detected using the same technique as the far-field experiments, using another photoconductive antenna (Protemics TeraSpike TD-800-X-HR-WT-XR) which can instead scan the sample surface. Our setup measures the x component of the electric field, using the reference frame of Figure 6. A moveable, fiber-coupled near-field detector module enables measurement of the electric field as a function of time at every point in the xz plane. A second harmonic generation (SHG) module (Protemics) converts the 1560 nm laser pulses to 780 nm to excite the low-temperature GaAs photocurrent on the antenna tip needed for terahertz detection. Fast Fourier transforms of the temporal response at each pixel position provide the spectral information. See Animation 1 in the Supporting Information for the full measurement associated with Figure 6(d).

ASSOCIATED CONTENT

Supporting Information

The Supporting Information is available free of charge at https://pubs.acs.org/doi/10.1021/acsnano.4c09434.

Simulations showing polarization rotation in the lower part of the gold-coated quartz waveguide (Figure S1); simulations comparing the field above the NGWG and below the SiWG with and without the nanogap (Figure S2); spatial Fourier analysis of the measured field in Figure 6 (Figure S3); electric field measurements below the SiWG (Figure S4); discussion of the estimated field intensity exiting the silicon waveguide (Figure S5); simulations estimating the fraction of power scattered by the nanogap waveguide (Figure S6); Drude–Lorentz model for the permittivity of gold (Table S1) (PDF)

Annotated animation associated with Figure 6(d) (Animation 1) (AVI)

AUTHOR INFORMATION

Corresponding Author

Alessandro Tuniz – *Commonwealth Scientific and Industrial Research Organisation (CSIRO), Lindfield, NSW 2070, Australia; Institute of Photonics and Optical Science (IPOS), School of Physics, The University of Sydney, Camperdown, NSW 2006, Australia;* orcid.org/0000-0002-3950-6282; Email: alessandro.tuniz@csiro.au

Authors

Sabrina Garattoni – *Dipartimento di Fisica, Politecnico di Milano, Milan 20133, Italy; Institute of Photonics and Optical Science (IPOS), School of Physics, The University of Sydney, Camperdown, NSW 2006, Australia*

Han-Hao Cheng – *Centre for Microscopy and Microanalysis, The University of Queensland, St Lucia, QLD 4072, Australia*

Giuseppe Della Valle – *Dipartimento di Fisica, Politecnico di Milano, Milan 20133, Italy;* orcid.org/0000-0003-0117-2683

Complete contact information is available at: https://pubs.acs.org/10.1021/acsnano.4c09434

https://doi.org/10.1021/acsnano.4c09434
ACS Nano 2024, 18, 30626–30637

Author Contributions

A.T. conceived the idea and directed the project. S.G. designed the silicon and nanogap waveguides and started the fabrication of the silicon waveguides. A.T. completed the fabrication of silicon waveguides and performed the experiments. H.-H.C. fabricated the nanogap waveguides. A.T. analyzed the experimental data, performed the final simulations, and wrote the manuscript. G.D.V. provided scientific guidance and revised the manuscript.

Notes

The authors declare no competing financial interest.

This work was previously submitted to a preprint server: Tuniz, A.; Garattoni, S.; Cheng, H.-H.; Della Valle, G. Directional coupling to a $\lambda/5000$ nanowaveguide. 2024, arXiv:2407.19620. arXiv. 10.48550/arXiv.2407.19620 (accessed September 30, 2024).

ACKNOWLEDGMENTS

This work was funded in part by the Australian Research Council Discovery Early Career Researcher Award (DE200101041). This work was performed in part at the NSW nodes of the Australian Nanofabrication Facility. We acknowledge the facilities, and the scientific and technical assistance, of the Australian Microscopy & Microanalysis Research Facility at the Centre for Microscopy and Microanalysis, The University of Queensland. In particular, we gratefully acknowledge Gloria Qiu and Jackie He from the University of Sydney for assistance with sample fabrication. A.T. thanks Boris T. Kuhlmey for fruitful discussions.

REFERENCES

(1) Markelz, A. G.; Mittleman, D. M. Perspective on Terahertz Applications in Bioscience and Biotechnology. *ACS Photonics* **2022**, *9*, 1117−1126.

(2) Smolyanskaya, O. A.; Chernomyrdin, N.; Konovko, A.; et al. Terahertz Biophotonics as a Tool for Studies of Dielectric and Spectral Properties of Biological Tissues and Liquids. *Prog. Quantum Electron.* **2018**, *62*, 1−77.

(3) Seo, C.; Kim, T.-T. Terahertz Near-Field Spectroscopy for Various Applications. *J. Korean Phys. Soc.* **2022**, *81*, 549−561.

(4) Siegel, P. H. THz Instruments for Space. *IEEE Trans. Antennas Propag.* **2007**, *55*, 2957−2965.

(5) Kleine-Ostmann, T.; Nagatsuma, T. A Review on Terahertz Communications Research. *J. Infrared, Millimeter, Terahertz Waves* **2011**, *32*, 143−171.

(6) Sizov, F.; Rogalski, A. THz Detectors. *Prog. Quantum Electron.* **2010**, *34*, 278−347.

(7) Pang, X.; Ozolins, O.; Jia, S.; Zhang, L.; Schatz, R.; Udalcovs, A.; Bobrovs, V.; Hu, H.; Morioka, T.; Sun, Y.-T.; Chen, J.; Lourdudoss, S.; Oxenløwe, L. K.; Popov, S.; Yu, X. Bridging the Terahertz Gap: Photonics-Assisted Free-Space Communications from the Submillimeter-Wave to the Mid-Infrared. *J. Lightwave Technol.* **2022**, *40*, 3149−3162.

(8) Headland, D.; Withayachumnankul, W.; Yu, X.; Fujita, M.; Nagatsuma, T. Unclad Microphotonics for Terahertz Waveguides and Systems. *J. Lightwave Technol.* **2020**, *38*, 6853−6862.

(9) Xu, G.; Skorobogatiy, M. Wired THz Communications. *J. Infrared, Millimeter, Terahertz Waves* **2022**, *43*, 728−778.

(10) Leitenstorfer, A.; Moskalenko, A. S.; Kampfrath, T.; Kono, J.; Castro-Camus, E.; Peng, K.; Qureshi, N.; Turchinovich, D.; Tanaka, K.; Markelz, A. G.; et al. The 2023 terahertz science and technology roadmap. *J. Phys. D: Appl. Phys.* **2023**, *56*, No. 223001.

(11) Lawler, N. B.; Ho, D.; Evans, C. W.; Wallace, V. P.; Iyer, K. S. Convergence of Terahertz Radiation and Nanotechnology. *J. Mater. Chem. C* **2020**, *8*, 10942−10955.

(12) Rosei, F. Nanostructured surfaces: challenges and frontiers in nanotechnology. *J. Phys.: Condens. Matter* **2004**, *16*, No. S1373.

(13) Chen, H.-T.; Kersting, R.; Cho, G. C. Terahertz imaging with nanometer resolution. *Appl. Phys. Lett.* **2003**, *83*, 3009−3011.

(14) Wittmann, S.; Pindl, S.; Sawallich, S.; Nagel, M.; Michalski, A.; Pandey, H.; Esteki, A.; Kataria, S.; Lemme, M. C. Assessment of wafer-level transfer techniques of graphene with respect to semiconductor industry requirements. *Adv. Mater. Technol.* **2023**, *8*, No. 2201587.

(15) Tuniz, A.; Kuhlmey, B. T. Subwavelength terahertz imaging via virtual superlensing in the radiating near field. *Nat. Commun.* **2023**, *14*, No. 6393.

(16) Guo, X.; Bertling, K.; Donose, B. C.; Brünig, M.; Cernescu, A.; Govyadinov, A. A.; Rakić, A. D. Terahertz nanoscopy: Advances, challenges, and the road ahead. *Appl. Phys. Rev.* **2024**, *11*, No. 021306, DOI: 10.1063/5.0189061.

(17) Cocker, T. L.; Jelic, V.; Hillenbrand, R.; Hegmann, F. Nanoscale terahertz scanning probe microscopy. *Nat. Photonics* **2021**, *15*, 558−569.

(18) Kaltenecker, K. J.; Gölz, T.; Bau, E.; Keilmann, F. Infrared-spectroscopic, dynamic near-field microscopy of living cells and nanoparticles in water. *Sci. Rep.* **2021**, *11*, No. 21860.

(19) Park, S.-G.; Jin, K. H.; Yi, M.; Ye, J. C.; Ahn, J.; Jeong, K.-H. Enhancement of terahertz pulse emission by optical nanoantenna. *ACS Nano* **2012**, *6*, 2026−2031.

(20) Peters, L.; Rocco, D.; Olivieri, L.; Leon, U. A.; Cecconi, V.; Carletti, L.; Gigli, C.; Valle, G. D.; Cutrona, A.; Gongora, J. S. T.; Leo, G.; Pasquazi, A.; De Angelis, C.; Peccianti, M. Resonant Fully Dielectric Metasurfaces for Ultrafast Terahertz Pulse Generation. *Adv. Opt. Mater.* **2024**, *12*, No. 2303148.

(21) Vitiello, M. S.; Coquillat, D.; Viti, L.; Ercolani, D.; Teppe, F.; Pitanti, A.; Beltram, F.; Sorba, L.; Knap, W.; Tredicucci, A. Room-temperature terahertz detectors based on semiconductor nanowire field-effect transistors. *Nano Lett.* **2012**, *12*, 96−101.

(22) Degl'Innocenti, R.; Kindness, S. J.; Beere, H. E.; Ritchie, D. A. All-integrated terahertz modulators. *Nanophotonics* **2018**, *7*, 127−144.

(23) Headland, D.; Fujita, M.; Carpintero, G.; Nagatsuma, T.; Withayachumnankul, W. Terahertz integration platforms using substrateless all-silicon microstructures. *APL Photonics* **2023**, *8*, No. 091101.

(24) Han, Z.; Zhang, Y.; Bozhevolnyi, S. I. Spoof surface plasmon-based stripe antennas with extreme field enhancement in the terahertz regime. *Opt. Lett.* **2015**, *40*, 2533−2536.

(25) Tsiatmas, A.; Fedotov, V. A.; de Abajo, F. J. G.; Zheludev, N. I. Low-loss terahertz superconducting plasmonics. *New J. Phys.* **2012**, *14*, No. 115006.

(26) Yang, J.; Cao, Q.; Zhou, C. Theory for terahertz plasmons of metallic nanowires with sub-skin-depth diameters. *Opt. Express* **2010**, *18*, 18550−18557.

(27) Salamin, Y.; Benea-Chelmus, I.-C.; Fedoryshyn, Y.; Heni, W.; Elder, D. L.; Dalton, L. R.; Faist, J.; Leuthold, J. Compact and ultra-efficient broadband plasmonic terahertz field detector. *Nat. Commun.* **2019**, *10*, No. 5550.

(28) Sengupta, K.; Nagatsuma, T.; Mittleman, D. M. Terahertz integrated electronic and hybrid electronic-photonic systems. *Nat. Electron.* **2018**, *1*, 622−635.

(29) Rajabali, S.; Benea-Chelmus, I.-C. Present and future of terahertz integrated photonic devices. *APL Photonics* **2023**, *8*, No. 080901.

(30) Park, H.-R.; Chen, X.; Nguyen, N.-C.; Peraire, J.; Oh, S.-H. Nanogap-enhanced terahertz sensing of 1 nm thick ($\lambda/10^6$) dielectric films. *ACS Photonics* **2015**, *2*, 417−424.

(31) Park, S. J.; Cha, S.; Shin, G.; Ahn, Y. Sensing viruses using terahertz nano-gap metamaterials. *Biomed. Opt. Express* **2017**, *8*, 3551−3558.

(32) Kim, N.; In, S.; Lee, D.; Rhie, J.; Jeong, J.; Kim, D.-S.; Park, N. Colossal terahertz field enhancement using split-ring resonators with a sub-10 nm gap. *ACS Photonics* **2018**, *5*, 278−283.

(33) Lee, D.-K.; Kang, J.-H.; Lee, J.-S.; Kim, H.-S.; Kim, C.; Hun Kim, J.; Lee, T.; Son, J.-H.; Park, Q.-H.; Seo, M. Highly sensitive and selective

sugar detection by terahertz nano-antennas. *Sci. Rep.* **2015**, *5*, No. 15459.
(34) Bahk, Y.-M.; Kim, D.-S.; Park, H.-R. Large-Area Metal Gaps and Their Optical Applications. *Adv. Opt. Mater.* **2019**, *7*, No. 1800426.
(35) Stegeman, G. I.; Wallis, R.; Maradudin, A. Excitation of surface polaritons by end-fire coupling. *Opt. Lett.* **1983**, *8*, 386−388.
(36) Taras, A. K.; Tuniz, A.; Bajwa, M. A.; Ng, V.; Dawes, J. M.; Poulton, C. G.; de Sterke, C. M. Shortcuts to adiabaticity in waveguide couplers−theory and implementation. *Adv. Phys.: X* **2021**, *6*, No. 1894978.
(37) Tuniz, A.; Song, A. Y.; Della Valle, G.; de Sterke, C. M. Coupled mode theory for plasmonic couplers. *Appl. Phys. Rev.* **2024**, *11*, No. 021309.
(38) Yu, X.; Kim, J.-Y.; Fujita, M.; Nagatsuma, T. Efficient mode converter to deep-subwavelength region with photonic-crystal waveguide platform for terahertz applications. *Opt. Express* **2019**, *27*, 28707−28721.
(39) Delacour, C.; Blaize, S.; Grosse, P.; Fedeli, J. M.; Bruyant, A.; Salas-Montiel, R.; Lerondel, G.; Chelnokov, A. Efficient directional coupling between silicon and copper plasmonic nanoslot waveguides: toward metal-oxide-silicon nanophotonics. *Nano Lett.* **2010**, *10*, 2922−2926.
(40) Nielsen, M. P.; Shi, X.; Dichtl, P.; Maier, S. A.; Oulton, R. F. Giant nonlinear response at a plasmonic nanofocus drives efficient four-wave mixing. *Science* **2017**, *358*, 1179−1181.
(41) Novotny, L.; Hecht, B. *Principles of Nano-optics*; Cambridge University Press: Cambridge, 2012.
(42) Seo, M. A.; Park, H.; Koo, S.; Park, D.; Kang, J.; Suwal, O.; Choi, S.; Planken, P.; Park, G.; Park, N.; et al. Terahertz field enhancement by a metallic nano slit operating beyond the skin-depth limit. *Nat. Photonics* **2009**, *3*, 152−156.
(43) He, X.-Y. Investigation of terahertz Sommerfeld wave propagation along conical metal wire. *J. Opt. Soc. Am. B* **2009**, *26*, A23−A28.
(44) Dai, J.; Zhang, J.; Zhang, W.; Grischkowsky, D. Terahertz Time-Domain Spectroscopy Characterization of the Far-Infrared Absorption and Index of Refraction of High-Resistivity, Float-Zone Silicon. *J. Opt. Soc. Am. B* **2004**, *21*, 1379−1386.
(45) Davies, C. L.; Patel, J. B.; Xia, C. Q.; Herz, L. M.; Johnston, M. B. Temperature-dependent refractive index of quartz at terahertz frequencies. *J. Infrared, Millimeter, Terahertz Waves* **2018**, *39*, 1236−1248.
(46) Rakić, A. D.; Djurišić, A. B.; Elazar, J. M.; Majewski, M. L. Optical properties of metallic films for vertical-cavity optoelectronic devices. *Appl. Opt.* **1998**, *37*, 5271−5283.
(47) Huang, W.-P. Coupled-mode theory for optical waveguides: an overview. *J. Opt. Soc. Am. A* **1994**, *11*, 963−983.
(48) Feng, L.; El-Ganainy, R.; Ge, L. Non-Hermitian photonics based on parity−time symmetry. *Nat. Photonics* **2017**, *11*, 752−762.
(49) Miri, M.-A.; Alù, A. Exceptional points in optics and photonics. *Science* **2019**, *363*, No. eaar7709.
(50) Tuniz, A.; Schmidt, M. A.; Kuhlmey, B. T. Influence of non-Hermitian mode topology on refractive index sensing with plasmonic waveguides. *Photonics Res.* **2022**, *10*, 719−730.
(51) Bogaerts, W.; Chrostowski, L. Silicon photonics circuit design: methods, tools and challenges. *Laser Photonics Rev.* **2018**, *12*, No. 1700237.
(52) Tuniz, A.; Schmidt, M. A. Broadband efficient directional coupling to short-range plasmons: towards hybrid fiber nanotips. *Opt. Express* **2016**, *24*, 7507−7524.
(53) Tuniz, A.; Wieduwilt, T.; Schmidt, M. A. Tuning the Effective PT Phase of Plasmonic Eigenmodes. *Phys. Rev. Lett.* **2019**, *123*, No. 213903.
(54) Akiki, E.; Verstuyft, M.; Kuyken, B.; Walter, B.; Faucher, M.; Lampin, J.-F.; Ducournau, G.; Vanwolleghem, M. High-Q THz photonic crystal cavity on a low-loss suspended silicon platform. *IEEE Trans. Terahertz Sci. Technol.* **2021**, *11*, 42−53.
(55) Verstuyft, M.; Akiki, E.; Vanwolleghem, M.; Ducournau, G.; Lampin, J.-F.; Walter, B.; Bavedila, F.; Lebouvier, É.; Faucher, M.; Kuyken, B. Short bends using curved mirrors in silicon waveguides for terahertz waves. *Opt. Express* **2022**, *30*, 6656−6670.
(56) Jepsen, P. U.; Cooke, D. G.; Koch, M. Terahertz Spectroscopy and Imaging: Modern Techniques and Applications. *Laser Photonics Rev.* **2011**, *5*, 124−166.
(57) Caspers, J. N.; Aitchison, J. S.; Mojahedi, M. Experimental demonstration of an integrated hybrid plasmonic polarization rotator. *Opt. Lett.* **2013**, *38*, 4054−4057.
(58) Tuniz, A.; Bickerton, O.; Diaz, F. J.; Käsebier, T.; Kley, E.-B.; Kroker, S.; Palomba, S.; de Sterke, C. M. Modular Nonlinear Hybrid Plasmonic Circuit. *Nat. Commun.* **2020**, *11*, No. 2413.
(59) Kim, S.; Qi, M. Polarization rotation and coupling between silicon waveguide and hybrid plasmonic waveguide. *Opt. Express* **2015**, *23*, 9968−9978.
(60) Stefani, A.; Kuhlmey, B. T.; Digweed, J.; Davies, B.; Ding, Z.; Zreiqat, H.; Mirkhalaf, M.; Tuniz, A. Flexible terahertz photonic light-cage modules for in-core sensing and high temperature applications. *ACS Photonics* **2022**, *9*, 2128−2141.
(61) Yang, Z.; Tang, D.; Hu, J.; Tang, M.; Zhang, M.; Cui, H.-L.; Wang, L.; Chang, C.; Fan, C.; Li, J.; Wang, H. Near-Field Nanoscopic Terahertz Imaging of Single Proteins. *Small* **2021**, *17*, No. 2005814.
(62) Rodrigo, D.; Limaj, O.; Janner, D.; Etezadi, D.; García de Abajo, F. J.; Pruneri, V.; Altug, H. Mid-infrared plasmonic biosensing with graphene. *Science* **2015**, *349*, 165−168.
(63) Tuniz, A. Nanoscale nonlinear plasmonics in photonic waveguides and circuits. *Riv.Nuovo Cimento* **2021**, *44*, 193−249.
(64) Herter, A.; Shams-Ansari, A.; Settembrini, F. F.; Warner, H. K.; Faist, J.; Lončar, M.; Benea-Chelmus, I.-C. Terahertz waveform synthesis in integrated thin-film lithium niobate platform. *Nat. Commun.* **2023**, *14*, No. 11.
(65) Groiseau, C.; Fernández-Domínguez, A. I.; Martín-Cano, D.; Muñoz, C. S. Single-photon source over the terahertz regime. *PRX Quantum* **2024**, *5*, No. 010312.
(66) Guo, X.; Ma, Y.; Wang, Y.; Tong, L. Nanowire plasmonic waveguides, circuits and devices. *Laser Photonics Rev.* **2013**, *7*, 855−881.
(67) Gacemi, D.; Mangeney, J.; Colombelli, R.; Degiron, A. Subwavelength metallic waveguides as a tool for extreme confinement of THz surface waves. *Sci. Rep.* **2013**, *3*, No. 1369.
(68) Hong, T.; Choi, K.; Ik Sim, K.; Ha, T.; Cheol Park, B.; Yamamori, H.; Hoon Kim, J. Terahertz electrodynamics and superconducting energy gap of NbTiN. *J. Appl. Phys.* **2013**, *114*, No. 243905.
(69) Siampour, H.; Kumar, S.; Davydov, V. A.; Kulikova, L. F.; Agafonov, V. N.; Bozhevolnyi, S. I. On-chip excitation of single germanium vacancies in nanodiamonds embedded in plasmonic waveguides. *Light: Sci. Appl.* **2018**, *7*, No. 61.
(70) Brückner, C.; Käsebier, T.; Pradarutti, B.; Riehemann, S.; Notni, G.; Kley, E.-B.; Tünnermann, A. Broadband Antireflective Structures Applied to High Resistive Float Zone Silicon in the THz Spectral Range. *Opt. Express* **2009**, *17*, 3063−3077.

https://doi.org/10.1021/acsnano.4c09434
ACS Nano 2024, 18, 30626−30637